

Ultra-low Power Microwave Oscillators based on Phase Change Oxides as Solid-State Neurons

B. Zhao,¹ J. Ravichandran,^{1,2*}

¹*Mork Family Department of Chemical Engineering and Materials Science, University of Southern California, Los Angeles, California, 90089, USA*

²*Ming Hsieh Department of Electrical Engineering, University of Southern California, Los Angeles, California, 90089, USA*

(Received:)

Neuro-inspired computing architectures are one of the leading candidates to solve complex, large-scale associative learning problems. The two key building blocks for neuromorphic computing are the synapse and the neuron, which form the distributed computing and memory units. Solid state implementations of these units remain an active area of research. Specifically, voltage or current controlled oscillators are considered a minimal representation of neurons for hardware implementations. Such oscillators should demonstrate synchronization and coupling dynamics for demonstrating collective learning behavior, besides the desirable individual characteristics such as scaling, power, and performance. To this end, we propose the use of nanoscale, epitaxial heterostructures of phase change oxides and oxides with metallic conductivity as a fundamental unit of an ultra-low power, tunable electrical oscillator capable of operating in the microwave regime. Our simulations show that optimized heterostructure design with low thermal boundary resistance can result in operation frequency of up to 3 GHz and power consumption as low as 15 fJ/cycle with rich coupling dynamics between the oscillators.

I. INTRODUCTION

As we approach the scaling limits of the digital logic based on von Neumann architecture [1], the available large computational power can be leveraged to solve associative learning problems such as pattern matching, image recognition [2, 3]. Alternative paradigms such as neuromorphic computing is considered efficient approaches to solve these problems and can lead to the proliferation of distributed and autonomous sensing, computing and communication platforms [4, 5]. Neuromorphic computing incorporates computation based on biological brain-inspired mechanisms, where the time series of signals are used to both modulate the memory elements and perform computations. This approach uses an interconnected network of neurons and synapses, where the neurons perform the distributed analog computing and the synapses act

*jayakanr@usc.edu

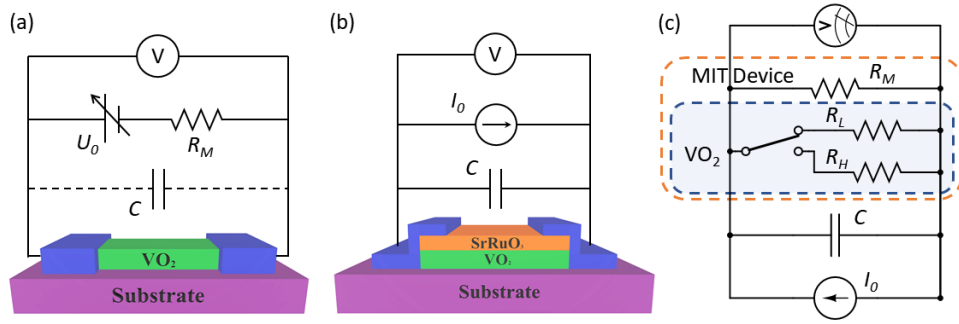


FIG. 1. Device structure and circuit diagram. (a) Schematic of the typical VO₂ electrical oscillator, where the VO₂ channel is connected in series to a known resistor and the Joule heat delivered to the series resistor adds to the extraneous power consumption, (b) Schematic of the proposed VO₂ based bilayer electrical oscillator with SrRuO₃ as the second layer. The bilayer is connected in parallel to a capacitor and current source is used to inject current into the device. (c) Schematic of the circuit diagram for the proposed oscillator device.

as the learning and memory units [6]. Early work on the hardware development based on neuromorphic computing relied heavily on the matured CMOS based platform [7]. However, recently approaches based on spin-torque [8, 9], metal-insulator-transition [10, 11], resistive switching [12], and ferroelectric phase change materials [13, 14] are being explored as alternatives to the traditional CMOS based ring oscillators.

Phase change materials showing metal-insulator transition (MIT), especially VO₂¹⁵, have been widely explored as a platform to achieve electrical oscillations [15, 16], often with oscillation frequency up to 9 MHz [17] and operation voltage below 1 V [18]. VO₂ undergoes a concomitant first-order structural [19] and electrical transition [20] with a large 5 orders of magnitude change in the electrical conductivity at 68°C in bulk single crystals [21]. Although the exact nature of the phase transition is still under considerable investigation [22-27], this large change in electrical conductivity [28] close to room temperature offers a novel method to create a feedback loop for switching between the metallic and insulating states, and hence, create electrical oscillations. The prototypical implementation of such an oscillator involves a VO₂ channel with lateral contacts connected to a series resistor and an external bias [29] (Fig. 1 (a)). In the insulating state, the Joule heating of the VO₂ channel effects a transformation to the metallic state. In the metallic state, the Joule heating is regulated by the external resistor and the available heating power is lower due to the low resistivity of the metallic state. This leads to cooling of the channel and recovery of the insulating state in VO₂. The highest oscillation frequency achieved in such devices was as high as 1 MHz with a power consumption of 1 nJ/cycle [30]. Recently, out-of-plane contact geometry to VO₂ channel was explored with a successful increase in the oscillator frequency to 9 MHz with a lower power consumption of 0.5 nJ/cycle [17]. A variation from both these geometries is the use of metal/VO₂ bilayer strips as oscillators [31]. Early attempts at using this geometry to induce electrical oscillations explored Pt/VO₂ bilayers [32]. These devices suffered from failure during repeated cycling and large thermal resistance at the Pt/VO₂ interface.

Several theoretical and experimental studies have shown that the time constant necessary for the metal-insulator transition can be as low as 2 ns and hence, one can achieve oscillation frequencies much higher than the observed 9 MHz in VO₂ based electrical oscillators [33-35]. Further, the current demonstrations suffer from large power consumption than what is necessary to induce the phase transition, which will limit their utility as low power oscillators [35]. To overcome the limitations of the current device designs discussed earlier, we propose an optimal VO₂-based oscillator device structure that can achieve both higher power efficiency and higher frequency without sacrificing any tunability compared to conventional electrical oscillators. Here, we report simulations of the heater-on-channel device structure for VO₂ based electrical oscillators (as shown in Fig. 1(b)) with minimal interface thermal boundary resistance to achieve

oscillation frequency as large as 3 GHz with a small power consumption of as low as 15 fJ/cycle. Our novel epitaxial bilayer device design minimizes the thermal time constant of the system by substantially reducing the active volume of material undergoing the metal-to-insulator transition. This not only leads to microwave oscillations but also reduces the power consumption drastically compared to earlier designs.

II. DEVICE STRUCTURE AND MECHANISM OF OPERATION

Our studies employ epitaxial bilayers of SrRuO₃ and VO₂ etched into a channel with lateral dimensions spanning 0.1-10 μm for length and width, and 5-30 nm for the thickness of each layer. As noted in Fig. 1(b), we will pass a current I_0 through the channel with a parallel capacitor with capacitance C to set up the oscillator. We carried out phenomenological modeling of the device operation to establish its performance metrics such as oscillation frequency, power consumption. The device is represented as a parallel bilayer system mounted on a semi-infinite substrate as the bilayer thickness is expected to be at least 3-4 orders of magnitude smaller than the substrate thickness. The phenomenological model consists of two constitutive equations that address the conservation of charge and heat energy in the system [31]. The conservation of charge is represented as a first-order differential equation as noted below:

$$I_0 = CdV/dt + V/R_{MIT} + V/R_M \quad (1)$$

where R_M and R_{MIT} are the resistances of the metallic oxide and VO₂ layer, and V is the voltage across the device. The equation representing the Newton's law of cooling (or the conservation of heat energy) is given below:

$$mC_m dT/dt = V^2/R_{MIT} + V^2/R_M - \kappa(T - T_0) \quad (2)$$

where m , C_m are the mass and heat capacity of the MIT device, T , T_0 are the temperature of the device and the ambient respectively, κ is the heat conductance between the device and the substrate. To solve these equations in a self-consistent manner, we have created a one-to-one map of the temperature and the resistance state of the VO₂ layer. As VO₂ undergoes a first-order transition, the specific resistance state of the material is dependent on whether channel is subject to the heating or cooling cycle (for detailed description please see Appendix A). Hence, we have ensured that this temperature-resistance map accounts for the hysteretic nature of the temperature dependence of resistance.

We performed finite element simulations of the temperature profile for the device channel to learn about the heat dissipation pathways and dominant thermal resistances. This analysis was used to identify the relevant contributions to the heat capacity and thermal resistance terms discussed in equation (2) (for detailed description please see Appendix A). Based on these calculations, we concluded that the dominant heat loss from the channel occurs *via* the substrate and the metal contacts. For the optimal device geometry with small heat capacity and small thermal resistance, one can achieve fast heating and cooling dynamics, which are the dominant rate-limiting steps for achieving fast electrical oscillations. We achieve this using a nanoscale mesa of ultrathin bilayers, where heat transfer is not fully limited by the thermal boundary resistance between the bilayer. Unless otherwise specified in the following discussions, we list all the relevant geometric and material parameters for the device in Table I.

TABLE I. Geometric dimensions, electrical and thermal properties of the materials used in the simulation

Property	Value	Property	Value
Thickness of VO ₂	5 nm	Density of SrRuO ₃	6490 kg/m ³
Thickness of SrRuO ₃	4 nm	Density of VO ₂	4570 kg/m ³
Channel Length	100 nm	Specific Heat of SrRuO ₃ [36]	650 J/kg K
Channel Width	100 nm	Specific Heat of VO ₂ [37]	690 J/kg K
Resistivity of SrRuO ₃ [38]	10 ⁻⁵ Ω m	Thermal conductivity of VO ₂ [37]	6 W/m K
Resistivity of VO ₂ (298K)	10 ⁻² Ω m	Thermal conductivity of Contacts (Pt)	70 W/m K
Resistivity of VO ₂ (400K)	4×10 ⁻⁷ Ω m	ITC of SrRuO ₃ /VO ₂ [39]	2×10 ⁸ W m ⁻² K ⁻¹
Temperature for IMT	345 K	ITC of SrRuO ₃ /Substrate [39]	1×10 ⁸ W m ⁻² K ⁻¹
Temperature for MIT	335 K	ITC of Channel/Contacts [40]	1×10 ⁷ W m ⁻² K ⁻¹

Note: IMT is metal-insulator transition; MIT is insulator-metal transition; ITC is the Interfacial thermal conductance.

Fig. 2(a) shows the time dependence of the voltage and temperature of the MIT device for operational parameters that achieve a median sustained oscillation frequency of ~3 GHz. The four regimes of operation are represented in the voltage and temperature oscillations by noting the relevant critical points: A, B, C, and D. A and C coincide with the crossover of the channel across the transition temperature, where the charging and discharging of the capacitors are triggered due to large changes to the channel resistance. B and D correspond to turning points in temperature, where the Joule heating and the heat dissipated are equal. As noted in the inset in Fig. 2(a), the power spectrum of the time-dependent voltage curve shows a peak at 3 GHz, which is the median frequency of the oscillations. The time taken by the device for the heating and cooling cycles were dependent on both the geometric and materials properties of the channel, and the operating current and capacitance values. Hence, one can tune the oscillation characteristics by changing these parameters. A closer look at the voltage oscillations shows that the DC component of these oscillations is minimal due to the large mismatch in the resistance between the metallic oxide and the metallic state of VO₂. This mismatch reduces the power consumption to an unprecedentedly low value of 15 fJ/pulse.

We compare the performance metrics such as power, frequency, and footprint of the proposed oscillator scheme with other state-of-the-art electrical oscillators in Table II. The widely used CMOS based oscillators (Ring Oscillators and RC Oscillators) have smaller size and improved tunability compared to bulky LC oscillators, but at the expense of increased power consumption. Resistive switching oscillators (RRAM Oscillators) have significantly smaller footprint compared to these schemes but suffer from lower frequency range and higher power consumption. Spin-torque oscillators are a simple and efficient oscillator scheme and produces highly tunable oscillations in a small footprint but consume large amounts of power. Current VO₂ technologies achieve low frequencies (~ MHz) with large power consumption but are very competitive in footprint compared to other schemes. Our proposed device can achieve superior metrics compared to all the other schemes considering the oscillator performance metrics.

TABLE II. Comparison with state-of-the-art oscillators

	Frequency (GHz)	Power (mW)	Power (fF/pulse)	Footprint (μm^2)
LC oscillator [41]	5.4	0.5	~ 92	0.18×10^6 [#]
Ring Oscillator [42]	3.35	1.45	~ 430	5600 [#]
RC Oscillator [43]	1.35×10^{-3}	0.92×10^{-3}	~ 680	5000 [#]
RRAM Oscillator [44]	0.5	0.25	~ 500	330 [#]
Spin Torque Oscillator [9]	0.33	~ 0.05	~ 151	0.14 [*]
Out-of-Phase VO ₂ [17]	9×10^{-3}	~ 4.5	$\sim 0.5 \times 10^6$	$\sim 1 \times 10^6$ [*]
In-Phase VO ₂ [30]	1×10^{-3}	~ 1.0	$\sim 1 \times 10^6$	40 [*]
Pt/VO ₂ Bilayer [32]	0.3×10^{-3}	~ 0.9	$\sim 3 \times 10^6$	1 [*]
This Work	3	0.045	15	0.01 [*]

Note: \sim Calculated or estimated from tables and figures; [#] Chip size; ^{*} Channel size;

One can learn about the mechanism of electrical oscillations by monitoring the Voltage-Current characteristics across the bilayer. In Fig. 2(b), we show the Voltage-Current (V-I) relationship for the oscillator channel, when sustained electrical oscillations are achieved. The plot clearly highlights four distinct regimes that constitute a single oscillation cycle. The regimes are: AB: charging, where supplied current is used to charge the capacitor; BC: heating, where current flows into the channel and heats the metallic layer to push the region of VO₂ channel right below the metal into the metallic state; CD: discharge, where the metallic VO₂ draws additional current from the capacitor by discharging it; and DA: cooling, where the metallic VO₂ doesn't have the necessary Joule heating power to sustain the metallic state, which leads to cooling and transition back to insulating state. These stages are achieved by moving clockwise in the V-I plot and continue in a cyclical manner to create sustained electrical oscillations until the external current supply continues to provide the power for the device.

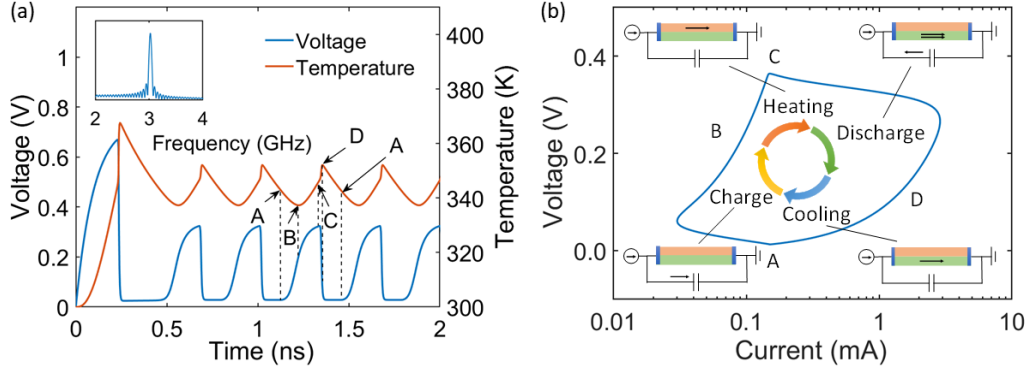


FIG. 2. Operation mechanism of the bilayer oscillator. (a) Simulated voltage-current (V-I) curve of the oscillatory cycle during the sustained oscillations in the device; the capacitance used was $C=1$ pF. The four stages of operation of the oscillator are charging, heating, discharging and cooling. The stages are represented in a clockwise manner with the color code used in the V-I curve corresponding to each stage described here. The stages are separated by four critical points: A, B, C and D. A and C represent the onset of the charging and discharging of the capacitor respectively, while B and D represent the onset of heating and cooling; (b) Time dependent variation of voltage and temperature of the MIT device for the highest achievable oscillation frequency of 3 GHz, since the start of the applied current. The different operating critical points within an oscillation are noted as A, B, C, and D as discussed in (a). The inset shows the power spectrum of the voltage oscillations that shows a dominant frequency of 3 GHz.

III. TUNIBILITY

Next, we discuss the tunability of the oscillator characteristics for the proposed device structure. We have several geometric, materials and operational parameters in our oscillator design that can tune the oscillation characteristics over several orders of magnitude. If one were to mimic the operation of a neuron using these oscillators, it is desirable to achieve tunability of the oscillation frequency, besides low power and high-frequency operation. To elucidate the key operating parameters for this device, we studied the effect of the parallel capacitance and the applied current on the oscillation frequency. The operating regime

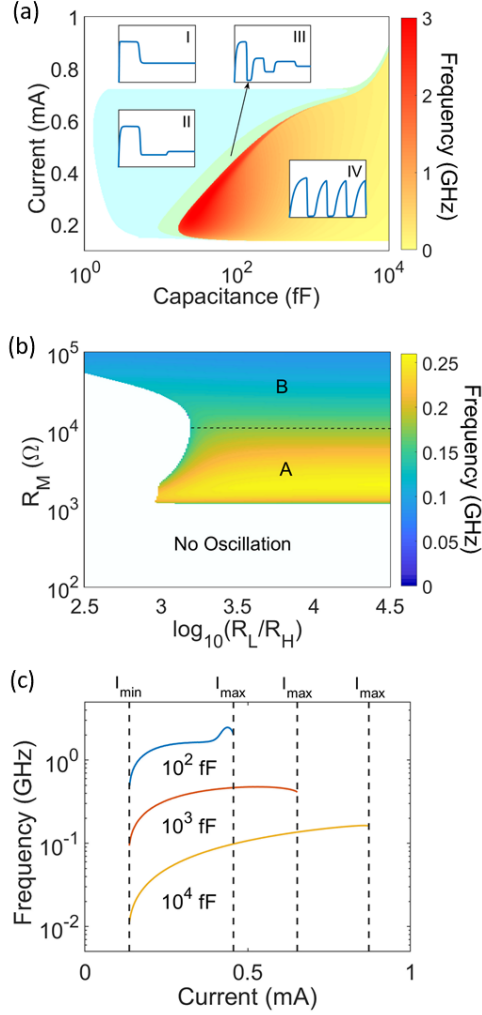


FIG. 3. Tunability of the bilayer oscillator. (a) Current-Capacitance phase diagram of the operating regimes of MIT based electrical oscillator. Region IV depicts fully sustained oscillators with the frequency range from 0-3GHz, time evolution of the voltage across the MIT device after the current is applied is characterized by: I – no oscillation; II – one oscillation; III – damped oscillations; IV – sustained oscillations; (b) The effect of the resistances of metallic oxide and MIT layer on the oscillator operation; The dominant parameters controlling the oscillation frequency in region I are R_M and R_H , and region II are R_L and R_H . ($C=1000$ fF, $I=0.2$ mA) (c) Frequency tunability by current and capacitance, $C=100$ fF, 1 pF and 10 pF; current ranges from I_{min} to I_{max} .

of the oscillator is represented as a current-capacitance phase diagram in Fig. 3(a). The phase diagram shows four distinct regimes, which are schematically shown. Regions I, II and III show no oscillation, one oscillation, and damped oscillations respectively. Once a threshold in the current and the capacitance is reached, we can enter region IV, where sustained oscillations are possible. In this regime, we can tune the oscillation frequency up to 3 GHz for the device parameters discussed in Table I. It is worth noting that if we modify the device parameters such as the channel area and thicknesses of the two layers in the bilayer, one can achieve finer tunability in the low-frequency regime down to MHz. As the higher frequency of operation in a solid-state neuron can reduce the need for higher scalability, we focus on achieving the highest possible frequency in the proposed device structure. We show the broad tunability of the oscillator frequency with current and the capacitance in Fig. 3(c). One can achieve a large tunability of a factor of 100 for changing capacitance with a constant current and a factor of 4 or more for changing current with constant capacitance. Specific example for these tunability ranges and the corresponding power spectrum are shown in Fig. 7(a) and (b) respectively in the high-frequency regime.

Another useful parameter to control the oscillation characteristics are the resistances of the individual layers in the bilayer channel. One of the easiest ways to control the resistance is by varying the thickness of the material. Growth conditions can be used to influence the resistivity of the VO₂ and SrRuO₃ layers too. The amplitude of the voltage oscillations is controlled by the total resistance of the bilayer channel. The voltage across the device for the two cases, where the VO₂ is in the insulating state and conducting states are given as:

$$V_{insulating} = I_0 R_M R_L / (R_M + R_L) \quad (3)$$

$$V_{conducting} = I_0 R_M R_H / (R_M + R_H) \quad (4)$$

where I_0 is the total current, R_M , R_L , R_H are the resistance of the SrRuO₃ layer, the low temperature (300K) insulating state of the VO₂ layer, the high temperature (400K) conducting state of the VO₂ layer. Fig. 3(b) shows the influence of R_M and the ratio between R_L and R_H on the oscillation frequency. In principle, all the three parameters could be varied, but the influence of the R_L on the oscillation characteristics was minimal, and hence, we chose to fix this value and studied the effect of R_M and R_H on the oscillation frequency. We do not observe any oscillations, when R_M is too small to heat up the device. Similarly, if R_H is higher than or comparable to R_M , one cannot establish a feedback loop that sets up the oscillation. The dominant parameters controlling the oscillation process in the two regions I and II are R_M and R_H , and R_L and R_H respectively. In region II, we simply recover the device operation for the scheme shown in Fig. 1(a) as R_M is very large and comparable to R_L . In other words, the surface layer acts as only a parasitic leakage in region II, but determines the frequency in region I. Clearly, a much higher frequency is achievable in Region I compared to Region II, which emphasizes the advantages of the bilayer device structure over the conventional series resistor-based device structure, provided the heat capacity and the thermal resistances are designed judiciously.

IV. SYNCHRONIZATION CHARACTERISTICS

Finally, we studied the nature of synchronization between two bilayer electrical oscillators, which is another key characteristic of a solid-state neuron. The coupling between the two electrical oscillators was controlled by a capacitor with capacitance, C_j , connecting the two oscillators. For these studies, we used the

difference in the current applied to each oscillator as the driving phase difference and the coupling capacitance as the measure of the strength of coupling between the oscillators. We generated the synchronization phase diagram for the oscillators (circuit diagram is shown in Fig. 4(a)), where driving oscillator has the applied current fixed at $I_1=0.25$ mA and the driven oscillator's current I_2 varied between 0.15 mA-0.45 mA for varying coupling capacitance ($C_i=0$ -100 fF). We mapped the frequency difference between the two oscillators after 10 ns to evaluate their ability to synchronize for a given driving phase and coupling strength and the resultant phase diagram is shown in Fig. 4(b). As noted, large capacitance leads to higher coupling strength and can synchronize oscillators that start with a large driving phase difference. We can also observe interesting synchronization trends for intermediate coupling, which demonstrates the richness of this time dynamics of these coupled oscillators.

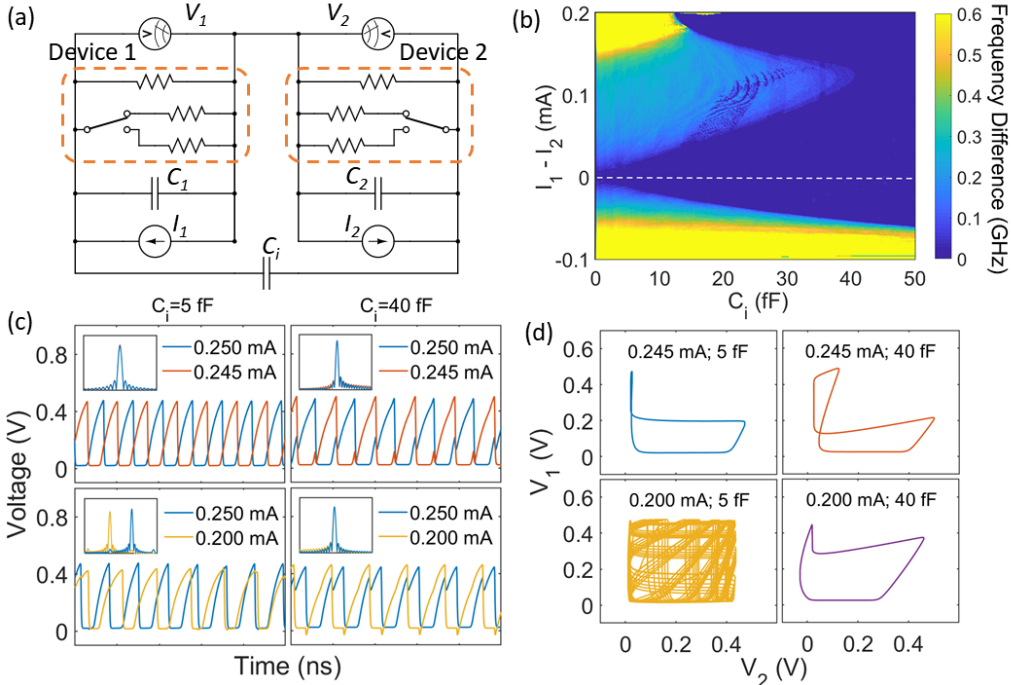


FIG. 4. Synchronization characteristics of coupled bilayer oscillators. (a) Schematic of the circuit diagram for two bilayer electrical oscillators connected in series for the synchronization studies; (b) The phase diagram of the synchronization characteristics between the two oscillators for different driving phase (difference in drive current) and coupling strength (coupling capacitance). One can notice the formation of the Arnold's tongue demonstrating the region where synchronization can be easily achieved and the oscillations lock in the same frequency even if they started with different frequencies. (c) Simulated voltage oscillations for two oscillators synchronizing or remaining out of sync with each other. The depicted time span is 10 ns to 15 ns. The inset shows the power spectrum of the oscillations for the two oscillators, which are locked in different frequencies when out of sync. (d) Phase maps for different I_1 and C_i combinations corresponding to (c) from 10 ns to 50 ns.

To demonstrate the synchronizing behavior in detail, we show the voltage oscillations for the two oscillators with a different driving phase difference ($I_1=0.250$ mA, $I_2=0.245$ mA; and $I_1=0.250$ mA, $I_2=0.200$ mA) and very different coupling strengths of $C_i=5$ fF and $C_i=40$ fF (Fig. 4(c)). The weak coupling strength of $C_i=5$ fF can synchronize a 0.005 mA current difference between the oscillators but is not sufficient to lock the driven oscillator with 0.050 mA current difference system into a stable oscillatory behavior. Stronger coupling allows one to achieve a more stable synchronized oscillatory behavior for the two oscillators. For example, when $C_i=40$ fF was used to couple the two oscillators, we could achieve synchronization for the driving phase differences of 0.005 mA and 0.050 mA. Phase maps under these

conditions are plotted in Fig. 4(d) (time span 10 ns to 50 ns). Clearly unsynchronized phase pattern is shown when $C_i=5$ fF was used to synchronize $I_1=0.250$ mA, $I_2=0.200$ mA. On the other hand, synchronized oscillators show anti-phase relationships in the other three circumstances. A deeper understanding of the nature of this synchronization between coupled oscillators is necessary to design the co-operative learning behavior of the network of oscillators.

V. CONCLUSION

In summary, we have introduced an ultra-low power, microwave electrical oscillators based on $\text{VO}_2/\text{SrRuO}_3$ bilayer heterostructures. Our proposed device structure is expected to have orders of magnitude higher frequency of operation and lower power consumption than current oscillator device structures. For an optimized device structure, we predict oscillation frequencies as high as 3 GHz and energy assumption as low as 15 fJ/pulse with a large dynamic and static tunability of the oscillator characteristics. The synchronization between two oscillators shows rich and complex dynamical behavior, which is a promising demonstration towards achieving large coupled oscillatory computational systems. This study lays the foundation for future theoretical and experimental studies towards scalable, ultra-lower power solid-state neurons capable of operating in the microwave regime for neuromorphic computing. More broadly, we envision that such ultra-low power tunable microwave oscillators can find application in fields spanning clocking, communication, sensing, and computing.

ACKNOWLEDGEMENTS

The authors gratefully acknowledge the support from the USC Viterbi School of Engineering startup funds and the Air Force Office of Scientific Research under award number FA9550-16-1-0335. We acknowledge the assistance of Yang Liu and Shanyuan Niu for careful reading of the manuscript and providing useful feedback. We also acknowledge helpful discussions with Asif Islam Khan, Rehan Kapadia, Han Wang, Priya Vashishta and Rajiv Kalia.

REFERENCES

- [1] D. J. Frank, R. H. Dennard, E. Nowak, P. M. Solomon, Y. Taur, and H. S. P. Wong, Device scaling limits of Si MOSFETs and their application dependencies, *Proceedings of the IEEE* **89**, 259 (2001).
- [2] S. B. Eryilmaz, D. Kuzum, R. Jeyasingh, S. Kim, M. BrightSky, C. Lam, and H. S. P. Wong, Brain-like associative learning using a nanoscale non-volatile phase change synaptic device array, *Frontiers in Neuroscience* **8**, 205 (2014).
- [3] A. Parihar, N. Shukla, M. Jerry, S. Datta, and A. Raychowdhury, Vertex coloring of graphs via phase dynamics of coupled oscillatory networks, *Scientific Reports* **7**, 911 (2017).
- [4] P. A. Merolla *et al.* A million spiking-neuron integrated circuit with a scalable communication network and interface, *Science* **345**, 668 (2014).
- [5] M. A. Lebedev and M. A. L. Nicolelis, Brain-machine interfaces: past, present and future, *Trends in Neurosciences* **29**, 536 (2006).
- [6] F. C. Hoppensteadt and E. M. Izhikevich, Oscillatory neurocomputers with dynamic connectivity, *Physical Review Letters* **82**, 2983 (1999).

- [7] K. H. Kim, S. Gaba, D. Wheeler, J. M. Cruz-Albrecht, T. Hussain, N. Srinivasa, and W. Lu, A Functional Hybrid Memristor Crossbar-Array/CMOS System for Data Storage and Neuromorphic Applications, *Nano Letters* **12**, 389 (2012).
- [8] K. Yogendra, D. L. Fan, and K. Roy, Coupled Spin Torque Nano Oscillators for Low Power Neural Computation, *IEEE Transactions on Magnetics* **51**, 4003909 (2015).
- [9] J. Torrejon *et al.* Neuromorphic computing with nanoscale spintronic oscillators, *Nature* **547**, 428 (2017).
- [10] P. Y. Chen, J. S. Seo, Y. Cao, S. M. Yu, and AcM, Compact Oscillation Neuron Exploiting Metal-Insulator-Transition for Neuromorphic Computing, in *35th IEEE/ACM International Conference on Computer-Aided Design (ICCAD)* Austin, TX, 2016).
- [11] L. Gao, P.-Y. Chen, and S. Yu, NbO_x based oscillation neuron for neuromorphic computing, *Applied Physics Letters* **111**, 103503 (2017).
- [12] A. A. Sharma, Y. L. Li, M. Skowronski, J. A. Bain, and J. A. Weldon, High-Frequency TaO_x-Based Compact Oscillators, *IEEE Transactions on Electron Devices* **62**, 3857 (2015).
- [13] Z. Wang, S. Khandelwal, and A. I. Khan, Ferroelectric Oscillators and Their Coupled Networks, *IEEE Electron Device Letters* **38**, 1614 (2017).
- [14] S. M. Yoon and H. Ishiwara, Adaptive-Learning Synaptic Devices Using Ferroelectric-Gate Field-Effect Transistors for Neuromorphic Applications, *Ferroelectric-Gate Field Effect Transistor Memories: Device Physics and Applications* **131**, 311 (2016).
- [15] A. Hajimiri and T. H. Lee, A general theory of phase noise in electrical oscillators, *IEEE Journal of Solid-State Circuits* **33**, 179 (1998).
- [16] H. T. Kim, B. J. Kim, S. Choi, B. G. Chae, Y. W. Lee, T. Driscoll, M. M. Qazilbash, and D. N. Basov, Electrical oscillations induced by the metal-insulator transition in VO₂, *Journal of Applied Physics* **107**, 023702 (2010).
- [17] M. S. Mian, K. Okimura, and J. Sakai, Self-oscillation up to 9 MHz based on voltage triggered switching in VO₂/TiN point contact junctions, *Journal of Applied Physics* **117**, 215305 (2015).
- [18] J. Q. Lin, K. Alam, L. Ocola, Z. Zhang, S. Datta, S. Ramanathan, S. Guha, and IEEE, Physics and Technology of Electronic Insulator-to-Metal Transition (E-IMT) for Record High On/Off Ratio and Low Voltage in Device Applications, 2017 IEEE International Electron Devices Meeting (IEDM) (2017).
- [19] S. Lee, I. N. Ivanov, J. K. Keum, and H. N. Lee, Epitaxial stabilization and phase instability of VO₂ polymorphs, *Scientific Reports* **6**, 19621 (2016).
- [20] M. Brahlek, L. Zhang, J. Lapano, H. T. Zhang, R. Engel-Herbert, N. Shukla, S. Datta, H. Paik, and D. G. Schlom, Opportunities in vanadium-based strongly correlated electron systems, *MRS Communications* **7**, 27 (2017).
- [21] Y. Muraoka and Z. Hiroi, Metal-insulator transition of VO₂ thin films grown on TiO₂ (001) and (110) substrates, *Applied Physics Letters* **80**, 583 (2002).
- [22] S. Biermann, A. Poteryaev, A. I. Lichtenstein, and A. Georges, Dynamical singlets and correlation-assisted peierls transition in VO₂, *Physical Review Letters* **94**, 026404 (2005).
- [23] N. B. Aetukuri *et al.* Control of the metal-insulator transition in vanadium dioxide by modifying orbital occupancy, *Nature Physics* **9**, 661 (2013).
- [24] M. M. Qazilbash *et al.* Mott transition in VO₂ revealed by infrared spectroscopy and nano-imaging, *Science* **318**, 1750 (2007).
- [25] G. Stefanovich, A. Pergament, and D. Stefanovich, Electrical switching and Mott transition in VO₂, *Journal of Physics-Condensed Matter* **12**, 8837 (2000).

- [26] G. Gopalakrishnan, D. Ruzmetov, and S. Ramanathan, On the triggering mechanism for the metal-insulator transition in thin film VO₂ devices: electric field versus thermal effects, *Journal of Materials Science* **44**, 5345 (2009).
- [27] J. Jeong, N. Aetukuri, T. Graf, T. D. Schladt, M. G. Samant, and S. S. P. Parkin, Suppression of Metal-Insulator Transition in VO₂ by Electric Field-Induced Oxygen Vacancy Formation, *Science* **339**, 1402 (2013).
- [28] H. Paik *et al.* Transport properties of ultra-thin VO₂ films on (001) TiO₂ grown by reactive molecular-beam epitaxy, *Applied Physics Letters* **107**, 163101 (2015).
- [29] Y. Taketa, F. Kato, M. Nitta, and M. Haradome, New Oscillation Phenomena in VO₂ Crystals, *Applied Physics Letters* **27**, 212 (1975).
- [30] N. Shukla *et al.* Synchronized charge oscillations in correlated electron systems, *Scientific Reports* **4**, 4964 (2014).
- [31] A. Stern, D. K. Efimkin, V. Galitski, Z. Fisk, and J. Xia, Radio Frequency Tunable Oscillator Device Based on a SmB₆ Microcrystal, *Physical Review Letters* **116**, 166603 (2016).
- [32] Y. Wang, J. W. Chai, S. J. Wang, L. Qi, Y. M. Yang, Y. J. Xu, H. Tanaka, and Y. H. Wu, Electrical oscillation in Pt/VO₂ bilayer strips, *Journal of Applied Physics* **117**, 064502 (2015).
- [33] Y. Zhou, X. N. Chen, C. H. Ko, Z. Yang, C. Mouli, and S. Ramanathan, Voltage-Triggered Ultrafast Phase Transition in Vanadium Dioxide Switches, *IEEE Electron Device Letters* **34**, 220 (2013).
- [34] D. S. Li, A. A. Sharma, D. K. Gala, N. Shukla, H. Paik, S. Datta, D. G. Schlom, J. A. Bain, and M. Skowronski, Joule Heating-Induced Metal-Insulator Transition in Epitaxial VO₂/TiO₂ Devices, *ACS Applied Materials & Interfaces* **8**, 12908 (2016).
- [35] Y. Zhang and S. Ramanathan, Analysis of "on" and "off" times for thermally driven VO₂ metal-insulator transition nanoscale switching devices, *Solid-State Electronics* **62**, 161 (2011).
- [36] F. Castelpoggi, L. Morelli, H. R. Salva, S. L. Cuffini, R. Carbonio, and R. D. Sanchez, Specific heat measurement of the magnetoresistant perovskite SrRuO₃, *Solid State Communications* **101**, 597 (1997).
- [37] D. W. Oh, C. Ko, S. Ramanathan, and D. G. Cahill, Thermal conductivity and dynamic heat capacity across the metal-insulator transition in thin film VO₂, *Applied Physics Letters* **96**, 151906 (2010).
- [38] G. Koster, L. Klein, W. Siemons, G. Rijnders, J. S. Dodge, C. B. Eom, D. H. A. Blank, and M. R. Beasley, Structure, physical properties, and applications of SrRuO₃ thin films, *Reviews of Modern Physics* **84**, 253 (2012).
- [39] R. B. Wilson, B. A. Apgar, W. P. Hsieh, L. W. Martin, and D. G. Cahill, Thermal conductance of strongly bonded metal-oxide interfaces, *Physical Review B* **91**, 115414 (2015).
- [40] T. Y. Lu, J. Zhou, T. Nakayama, R. G. Yang, and B. W. Li, Interfacial thermal conductance across metal-insulator/semiconductor interfaces due to surface states, *Physical Review B* **93**, 085433 (2016).
- [41] D. Murphy, H. Darabi, and IEEE, A Complementary VCO for IoE that Achieves a 195dBc/Hz FOM and Flicker Noise Corner of 200kHz, in *63rd IEEE International Solid-State Circuits Conference (ISSCC)* San Francisco, CA, 2016), pp. 44.
- [42] S. Yang, J. Yin, P. I. Mak, and R. P. Martins, A 0.0056mm all-digital MDLL using edge re-extraction, dual-ring VCOs and a 0.3mW block-sharing frequency tracking loop achieving 292fs Jitter and -249dB FOM, in *2018 IEEE International Solid - State Circuits Conference - (ISSCC)2018*, pp. 118.

- [43] A. Savanth, J. Myers, A. Weddell, D. Flynn, and B. Al-Hashimi, A 0.68nW/kHz Supply-Independent Relaxation Oscillator with $\pm 0.49\%/V$ and 96ppm/ $^{\circ}C$ Stability, in *2017 IEEE International Solid-State Circuits Conference (ISSCC)2017*, pp. 96.
- [44] T. C. Jackson, A. A. Sharma, J. A. Bain, J. A. Weldon, and L. Pileggi, Oscillatory Neural Networks Based on TMO Nano-Oscillators and Multi-Level RRAM Cells, *IEEE Journal on Emerging and Selected Topics in Circuits and Systems* **5**, 230 (2015).

APPENDIX A. METHODS AND SIMULATION APPROACH

I. Temperature Distribution

We considered the case of an oscillator device etched into a mesa structure and contacted by metal contacts on both the edges (Fig. 1(b) in main text) to learn about the dominant thermal resistances in the system. Due to comparable dimensions of length and width, we assumed that the temperature distribution along the width is uniform. We employed finite element modeling to learn about the temperature distribution along the length of the device (as shown in Fig. 6). We discretized the device into 10 nm (length) x 1 nm (thickness) blocks and each block was assigned a self-consistent temperature, and associated physical properties such as density, specific heat, resistivity, in-plane thermal conductivity and out-of-plane thermal conductivity for each layer (Table I). We included a semi-infinite substrate and 50 nm long contacts with relevant properties. Interfacial thermal conductance was set to the blocks at the interfaces and gave corresponding temperature drops. The temperature of the boundary of the device was fixed to $T_0=300K$. A time domain finite element simulation was carried out in MATLAB, beginning from a uniform temperature $T_0 = 300K$ with a time step $\Delta t = 10 fs$. Conservation of energy was represented by the following partial differential equation:

$$\rho c_p \partial T / \partial t = \nabla \cdot (k \nabla T) + E^2 / \rho_r \quad (5)$$

where ρ is volumetric mass density, c_p -specific heat, k -thermal conductivity, E -electric field, and ρ_r is the resistivity.

II. Resistance of VO₂.

The resistance of VO₂ layer (R_{MIT}) was obtained by adding the parallel resistances of VO₂ under different temperatures according to the temperature profile as shown in Fig. 6. The resistance of each layer was calculated as a function of their temperature as shown in Fig. 5.

III. Oscillator Characteristics.

The governing equations for the operation of the oscillator are listed as (1) and (2). The initial state is set to be $V = 0, I = 0, T(0) = 300K$. A time domain finite element simulation is carried out with time step $\Delta t = 100 fs$.

IV. Synchronization of Coupled Oscillators.

The synchronization between the oscillators was simulated using governing equations that obey Newton's law of cooling and the conservation of charge relationships:

$$I_1 = C_1 dV_1/dt + V_1/R_{MIT1} + V_1/R_{M1} + C_i d(V_1 - V_2)/dt \quad (7)$$

$$I_2 = C_2 dV_2/dt + V_2/R_{MIT2} + V_2/R_{M2} + C_i d(V_2 - V_1)/dt \quad (8)$$

Initial states of two oscillators are both set to be $V = 0, I = 0, T(0) = 300K$. Two oscillators are set to have different current input. A time sequence finite element simulation is carried out with time step $\Delta t = 100$ fs.

V. Resistivity of VO₂

Fig. 5 shows the temperature dependence of resistivity of VO₂ used in the simulation, which is representative of epitaxial VO₂ thin films.[19, 20, 27, 28] Transition temperature during heating was used as 345K (IMT temperature), while that during the cooling was 335K (MIT temperature). Four orders of magnitude change in resistivity were assumed across transition temperature. Resistivity during the heating

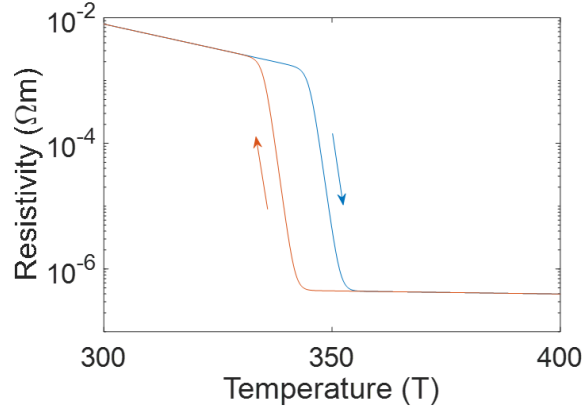


FIG. 5. The temperature dependent resistivity of VO₂. We used different transition temperature for heating and cooling cycles as expected for a first order phase transition.

or cooling cycle were considered differently in the simulation.

VI. Temperature Profile

Fig. 6 shows the simulated temperature map across the cross-section of the MIT channel. As the contact and the substrate are metallic with large conductivity and semi-infinite, their temperature remains almost constant at $T=T_0$ as the channel is heated up. This ensures excellent heat sinking for the heating powers considered in this study and therefore, the temperature profiles and dominant resistances considered remain the same over the whole operating regime. As Fig. 6 indicates, the temperature is uniform across the width and has a parabolic distribution across the length. IMT takes place at the interface between the bilayer, especially at the center of the VO₂ channel and proceeds from top to bottom. The progression of MIT follows the reverse course.

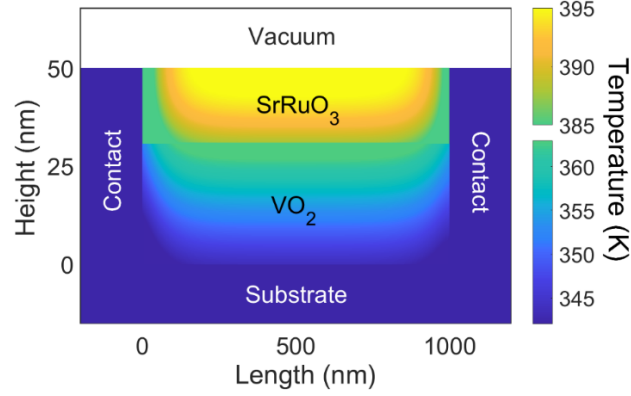


FIG. 6. Temperature profile for the cross section of the channel. The channel dimension was length = 1 μm , width = 1 μm , thickness of VO_2 = 30 nm, thickness of SrRuO_3 = 20 nm ($V=1.5$ V, $t = 10$ ns).

VII. Tunability

Fig. 7 shows the capacitor and current tunability and power spectrum for certain conditions near the highest frequency region in Fig 3(a). Fig. 7(a) shows the frequency tunability at $I_0=2$ mA. About two orders of magnitude difference of frequency can be achieved with the tuning of capacitance from 20 fF to 10 pF. Small changes in capacitance, on the other hand, changes the frequency linearly. Fig. 7(b) shows the frequency tunability at $C=100$ fF. The frequency increased by 3 times from I_{min} to I_{max} . The frequency peaks near I_{max} before the current input is too high for the channel to cool down.

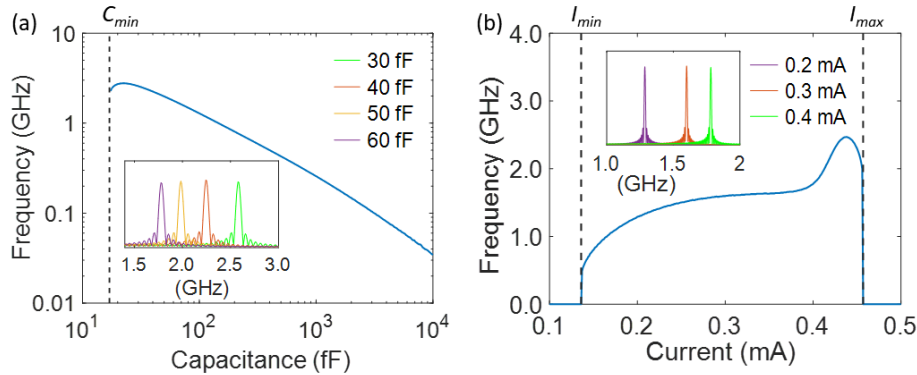


FIG. 7. Capacitor and current tunability and power spectrum near the highest frequency region (a) Frequency tuned by capacitance, $I_0=2$ mA; (b) Frequency tuned by current, $C=100$ fF.